

Modeling the impact of grid-forming E-STATCOMs on inter-area system oscillations.

A. Bolzoni^{*}, N. Johansson[†], J. P. Hasler^º

HITACHI ENERGY

^{*}Hitachi Energy Research, Segelhofstrasse, Baden Dättwil (CH)

[†] Hitachi Energy Research, Vaesteras (SE)

^º Grid and Power Quality Solutions, Hitachi Energy, Vaesteras (SE).

E-Mail: alberto.bolzoni@hitachienergy.com

URL: <https://www.hitachienergy.com/>

Keywords

«Frequency Dynamics», «Inertia support», «Converter control», «STATCOM», «FACTS».

Abstract

The reduction of physical inertia in power systems represents one of the major trends affecting public grids operations. Under this scenario, it becomes crucial to assess the positive contribution achievable through the application of advanced control strategies to converter-based units at the transmission and distribution levels. In this perspective, this paper analyzes how the introduction of grid-forming control functionalities in STATCOM devices could help toward the stabilization of the network transients and the reduction of inter-area phenomena.

Introduction

Low-inertia operations for power networks are becoming increasingly common, due to the replacement of synchronous machines supplied by fossil fuel power plants, and their substitution with renewable generators. A typical issue related to the reduced inertia is the amplification of inter-area oscillations: according to the definition proposed by the IEEE Power System Dynamics and CIGRE 38 study committees [1], these phenomena are defined as the relative swings between the phase angles of distant generators and may potentially lead to uncontrolled large-scale stability disruptions and to a reduction of the quality of the power supply. These oscillations are excited by a local and temporary mismatch between generation / consumption in one of the areas of the system and are characterized by a resonance angular frequency of around 0.2 – 2.5 rad/s [2]-[3].

In recent years, several authors analyzed the possibility to mitigate inter-area phenomena through diverse technologies like decentralized [4] or coordinated [5] control architectures for wind production plants, and Wide Area Monitoring infrastructures [6]. Another alternative consists in equipping the STATCOM devices installed at the transmission level with grid-forming control functionalities and with a supercapacitor storage placed at the DC side of the converter; this leads to the so called Enhanced-STATCOM (E-STATCOM) architecture.

This paper deals with the impact of E-STATCOM technology towards inter-area phenomena damping. More specifically, the goals are the following: to show how these devices manage to improve the stability of the network during transients; to derive an analytical model of the E-STATCOMs effect on inter-area modes; to assess the impact of the grid-forming scheme toward network stabilization; to provide some insights in the E-STATCOM best placement expressed as a function of the installation area.

To this purpose, a simple two-area configuration derived from [7] (and often referred as Kundur network) is considered; although simple, the architecture has been successfully exploited to test the positive effect of novel electronic devices on network system stability and inter-area phenomena [8]. DigSilent PowerFactory is used as simulation software for the analysis.

System modeling

Simplified transients' modeling

Consider the simple four-generator, two-area Kundur network typically exploited to study the impact of inter-area phenomena (Figure 1a). A simple representation of the active exchanges between the constituent areas is firstly introduced; this hypothesis will be later relaxed and a more general model able to include active / reactive dynamics and their inherent couplings will be presented in the next section.

The graphical representation in Figure 1b provides a simple representation of the dynamics occurring within and between the areas. Whenever a small local power mismatch is experienced in any of the two areas (Δp_{A1} or Δp_{A2}), the entire network undergoes a transitory condition: the regulation provided by local synchronous generators is combined with the power component Δp_{12} exchanged between the areas. Each of the areas {A1; A2} is modelled as an equivalent synchronous machine with starting time T_a (equal to twice the inertia constant H) and steady-state primary frequency control determined by the inverse droop coefficient r_{droop} . A common per-unit system (V_b : phase-to-phase per-unit base voltage 400 kV, S_b : per-unit base power 1800 MVA, ω_b : base angular frequency $2\pi \cdot 50$ rad/s) is adopted to enable homogenous calculations, and the actual characteristics of the specific areas can be referred to the base system as $T_a^{Ai} = T_a^{Ai'} \cdot S'_b/S_b$, $r_{droop}^{Ai} = r_{droop}^{Ai'} \cdot S'_b/S_b$, $i \in \{1,2\}$ (primed parameters stand for the original quantities, before they are referred to the common base system).

In addition to the inertial (T_a) and frequency regulation (r_{droop}) effects, the model includes the dynamics of the steam turbine and machine governors for the two areas through the following time constants: τ_1 , internal governor delay; τ_2 , derivative compensation of steam turbine delay; τ_3 , internal delay associated to the turbine control. The full set of parameters for the setup is provided in Tables 1-3.

Table 1: Ratings of synchronous generators and network

Synchronous generators ratings (same for each synchronous gen.)	Numeric value
Rated apparent power [MVA]	900
Rated transformer ratio [kV / kV] and short-circuit voltage [%]	400 / 20 – 15%
Connecting impedance between the two areas \bar{Z}_{12} [Ω]	$13.25 + j 132.5$

Table 2: Frequency regulation parameters for synchronous generators

Synchronous generators characteristics	Area 1 (G1 – G2)	Area 1 (G3 – G4)
Machine starting time T_a ($T_a = 2H$) [s]	6	10
Turbine gov. time constant τ_1 [s]	0.5	2
Turbine derivative time constant τ_2 [s]	1	5
Turbine delay time constant τ_3 [s]	3	5
Inverse droop coefficient r_{droop} [pu]	10	10

Table 3: E-STATCOM parameters

E-STATCOM characteristics	E-STAT 1 / E-STAT 2
Rated apparent power S_c [MVA]	500 MVA
Additional inertia H_{stat} [s] and additional damping term D_{stat} [s]	20 s, 0.3 s
Virtual admittance terms X_v [pu] - R_v [pu]	0.44 - 0.1
E-STATCOM supercapacitor parameters	1.78 F – 40 kV

In case each single area $i \in \{1,2\}$ operates independently of the other, the frequency dynamics under a load power increase Δp_{Ai} are expressed by:

$$\frac{\Delta\omega_{Ai}}{\Delta p_{Ai}} = K_{\omega_P}^{Ai}(s) = -\frac{(s\tau_1^{Ai} + 1)(s\tau_2^{Ai} + 1)}{sT_a^{Ai} (s\tau_1^{Ai} + 1)(s\tau_2^{Ai} + 1) + (s\tau_3^{Ai} + 1)r_{droop}^{Ai}}, \quad i \in \{1,2\}. \quad (1)$$

Once the areas are connected through the impedance \bar{Z}_{12} , the exchanged power Δp_{12} should also be included. Figure 1b shows the equivalent feedbacks (in blue, in the picture) associated to inter-area power exchange Δp_{12} proportional to the phase angle difference between the areas. For simplicity, here it is assumed a predominantly inductive impedance $\bar{Z}_{12} \simeq jX_{12}$: this hypothesis will be later removed in the complete model. Phase angles deviations (from steady-state values) $\Delta\vartheta_{A1}/\Delta\vartheta_{A2}$ are introduced for the two areas, defined as the integral of the local angular frequencies $\Delta\omega_{A1}/\Delta\omega_{A2}$.

$$\Delta p_{12} = \frac{V_1 V_2}{X_{12}} \sin(\Delta\vartheta_{A1} - \Delta\vartheta_{A2}) \simeq \frac{V_1 V_2}{X_{12}} (\Delta\vartheta_{A1} - \Delta\vartheta_{A2}) \quad (2)$$

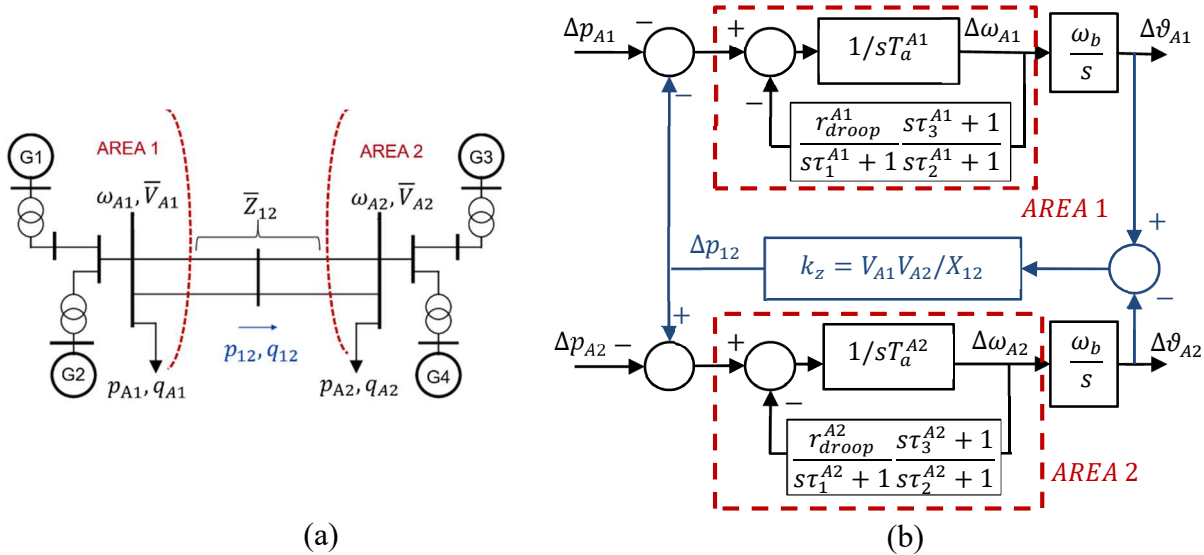


Fig. 1: (a) equivalent circuit for the two-area network setup and (b) simplified dynamic system for the modeling of active power exchanges in the test network. Constant-power models are used for the loads.

The dynamics of the interconnected system under possible active load variations at the two sides are expressed by the MIMO (Multi-Input Multi-Output) transfer matrix $\underline{G}(s)$ in (3), whose elements account for the active power interactions between the two areas; the term k_z exploited in (3) is equal to $k_z = V_{A1} V_{A2} / X_{12}$ and it is derived from (2).

$$\begin{bmatrix} \Delta\omega_{A1} \\ \Delta\omega_{A2} \end{bmatrix} = -\underline{G}_{2 \times 2}(s) \begin{bmatrix} \Delta p_{A1} \\ \Delta p_{A2} \end{bmatrix} \quad (3)$$

$$G_{ii}(s) = K_{\omega_P}^{Ai}(s) \left(1 + K_{\omega_P}^{Ai}(s) \frac{k_z \omega_b}{s} \left(1 + K_{\omega_P}^{Aj}(s) \cdot \frac{k_z \omega_b}{s} \right)^{-1} \right)^{-1} \quad i = \{1,2\}, \quad j \neq i \quad (3.b)$$

$$G_{ij}(s) = \frac{K_{\omega_P}^{Ai}(s) K_{\omega_P}^{Aj}(s) k_z \omega_b}{s + K_{\omega_P}^{Aj}(s) k_z \omega_b} \left(1 + \frac{K_{\omega_P}^{Ai}(s) K_{\omega_P}^{Aj}(s) \frac{k_z \omega_b^2}{s^2}}{1 + K_{\omega_P}^{Aj}(s) \frac{k_z \omega_b}{s}} \right)^{-1} \quad i = \{1,2\}, \quad j \neq i \quad (3.c)$$

The comparison between the Bode diagrams of the separate areas functions $K_{\omega_P}^{A1}(s)$ and $K_{\omega_P}^{A2}(s)$ from (1) against the elements of the transfer matrix $\underline{G}(s)$ (like $G_{11}(s)$ in Figure 2.a) shows the amplification of a resonance point in the equivalent regulation curve of the system. This resonance condition is the

source of the inter-area oscillations, and its natural frequency T_2^{-1} (in Hz) is marked in Fig. 2.a (where $T_2 \approx 1.4$ s from Fig. 2.b). The local maxima in the magnitude profile of $G_{11}(s)$ matches with the dominant harmonic components identifiable in the time profiles of $\Delta\omega_{A1}/\Delta\omega_{A2}$, confirming the correctness of the proposed modeling.

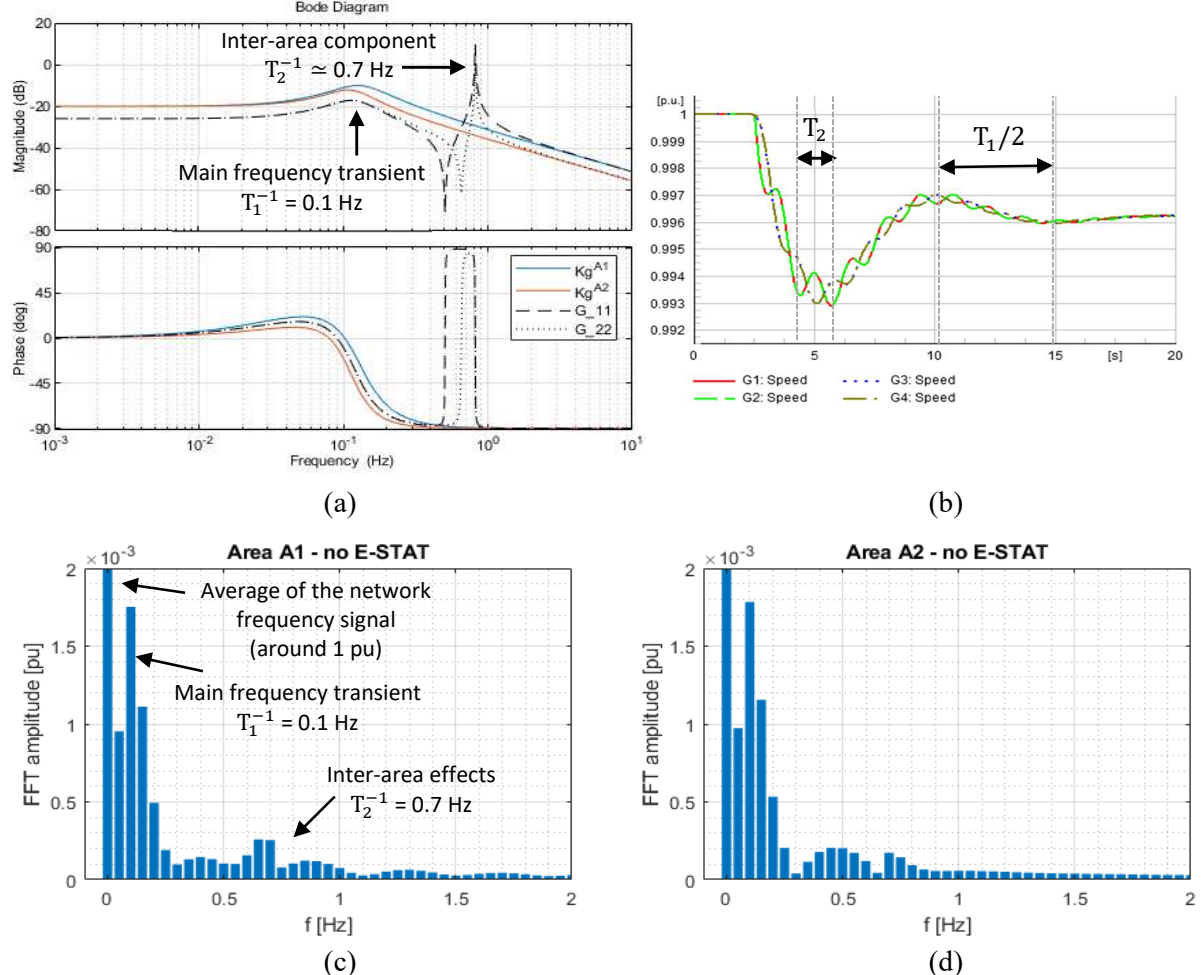


Fig. 2: (a) comparison between the equivalent regulation characteristics of the independent areas $K_g^{A1}(s)$ / $K_g^{A2}(s)$ and the ones resulting from the areas interconnection (represented by the term $G_{11}(s)$ and $G_{22}(s)$ in the MIMO-system); (b) the time profiles from DigSilent PowerFactory for $\Delta\omega_{A1}$ and $\Delta\omega_{A2}$ under a step change Δp_{A1} . The spectral decomposition of the local frequency signals at the two areas are also reported in (c) and (d), as an additional verification.

Extended MIMO model for assessment of the E-STATCOM effect.

Although the simple configuration reported in the previous subsection provides interesting insights in the core dynamical principles of inter-area phenomena, the assessment of the impact of the E-STATCOM technology requires an extensive modeling of the active / reactive power interaction between the converter-based units and the network. A full MIMO extension of the system is thus developed for this purpose; in this context, the grid-forming E-STATCOM is controlled to provide just inertial support, with no proportional frequency droop.

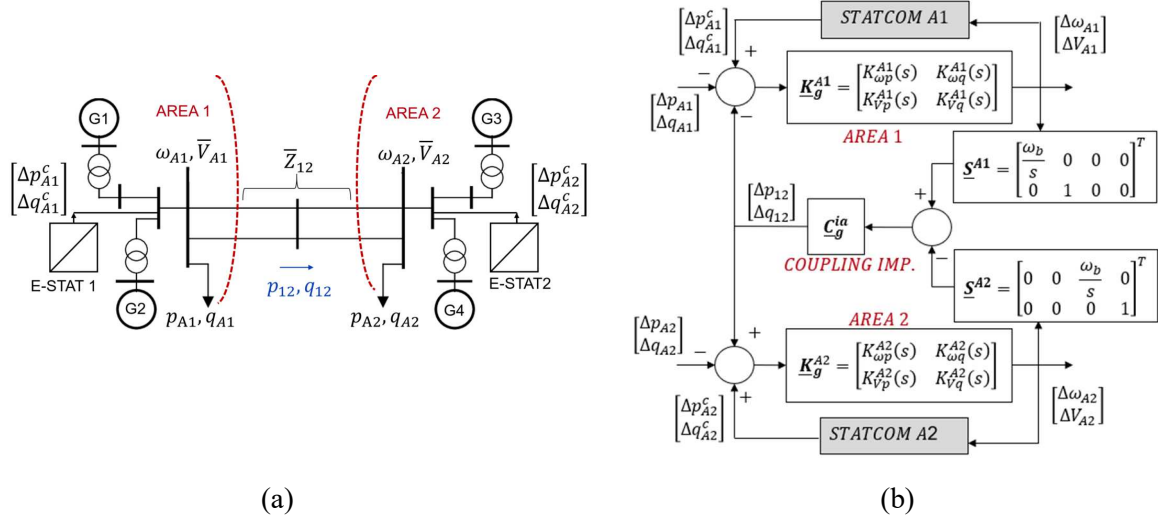


Fig. 3: MIMO model of the network for the assessment of E-STATCOM impact.

Figure 3 extends the approach introduced in Figure 1 to the generalized case of non-perfect decoupling between active and reactive power dynamics. The first step for the model development consists of deriving the natural response of the areas when just the loads and synchronous generators are connected (no E-STATCOMs). Extending the simple modeling introduced in (1), the area characteristics are now expressed through the 2×2 transfer matrix \underline{K}_g in (4).

The elements of \underline{K}_g can be derived either through analytical considerations or through system identification tests performed on the separate areas. In the DigSilent environment, the two areas are disconnected and characterized separately looking at their dynamical response following a local load step. The analytical formulation (1) is exploited to model the element $K_{\omega p}^{Ai}(s)$ in \underline{K}_g , while the remaining elements of the matrix are obtained through system identification. Figure 4 shows profiles of the simulated transients and their reconstructed analytical behavior ones under separate active / reactive steps for each of the two areas. As an alternative to the system identification, a more detailed modeling of the generators damper windings and PSS (Power-System Stabilizers) available in the time-domain simulation could be introduced.

$$\begin{bmatrix} \Delta\omega_{Ai} \\ \Delta V_{Ai} \end{bmatrix} = -\underline{K}_g^{2 \times 2}(s) \begin{bmatrix} \Delta p_{Ai} \\ \Delta q_{Ai} \end{bmatrix} = -\begin{bmatrix} K_{\omega p}^{Ai}(s) & K_{\omega q}^{Ai}(s) \\ K_{Vp}^{Ai}(s) & K_{Vq}^{Ai}(s) \end{bmatrix} \begin{bmatrix} \Delta p_{Ai} \\ \Delta q_{Ai} \end{bmatrix} \quad i \in \{1,2\} \quad (4)$$

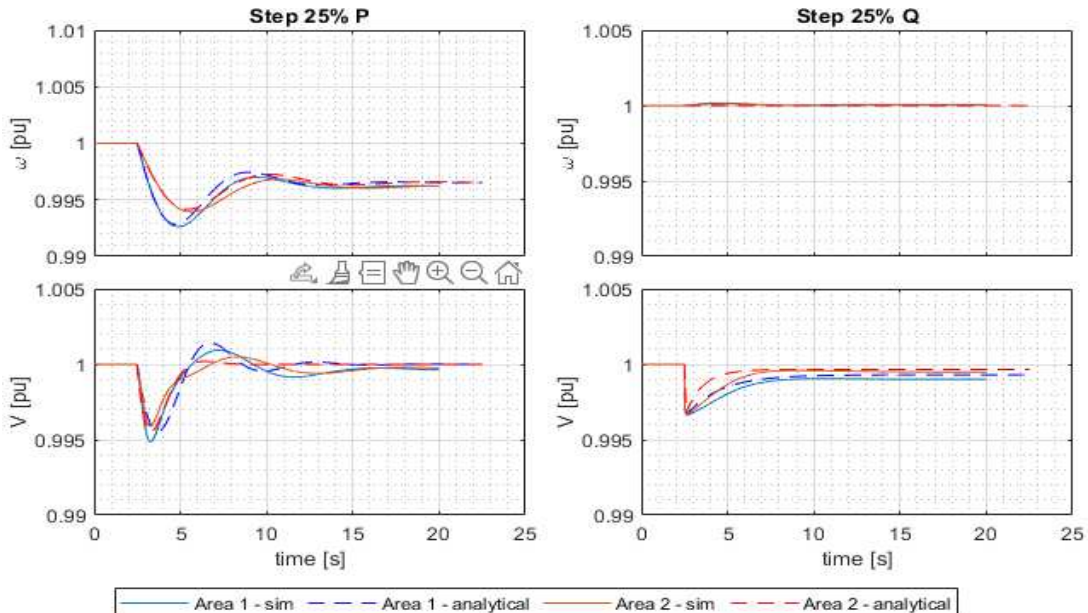


Fig. 4: Characterization of the two areas.

The local characteristics for each area are later combined to account for the inter-area exchanges $\Delta p_{12} / \Delta q_{12}$. This can be through the sensitivity matrixes $\underline{S}^{A1} / \underline{S}^{A2}$ (as defined in Figure 3.b) and the coupling matrix $\underline{\mathcal{C}}_g^{ia}$: this last element includes the linearized effects of the power flow equations [7] along the inter-area tie line which, for the generic case of ohmic-inductive impedance $\bar{Z}_{12} = R_{12} + jX_{12}$, is:

$$\underline{\mathcal{C}}_g^{ia} = \begin{bmatrix} \frac{V_1 V_2 X_{12}}{X_{12}^2 + R_{12}^2} & \frac{(2V_1 - V_2)R_{12}}{X_{12}^2 + R_{12}^2} & \frac{V_1 V_2 X_{12}}{X_{12}^2 + R_{12}^2} & \frac{V_1 R_{12}}{X_{12}^2 + R_{12}^2} \\ -\frac{V_1 V_2 R_{12}}{X_{12}^2 + R_{12}^2} & \frac{(2V_1 - V_2)X_{12}}{X_{12}^2 + R_{12}^2} & -\frac{V_1 V_2 R_{12}}{X_{12}^2 + R_{12}^2} & \frac{V_1 X_{12}}{X_{12}^2 + R_{12}^2} \end{bmatrix}. \quad (5)$$

An active / reactive power increase in one of the two areas impacts the voltage / frequency transients in each of the parts of the interconnected system. This case can be described through the MIMO system (6), assuming, as a base case, no contribution from the E-STATCOMs: the transfer matrix $\underline{\mathbf{G}}_{4 \times 4}^{\text{no STAT}}$ describes the dynamics generated by any active / reactive load variation on the frequency / voltage dynamics of each area.

The frequency response of $\underline{\mathbf{G}}_{4 \times 4}^{\text{no STAT}}$ provides insights in which area is potentially more affected by the inter-area resonance. In the specific case study, the shape of $\underline{\mathbf{G}}_{4 \times 4}^{\text{no STAT}}$ indicates that area A1 is potentially affected by larger swings of the voltage phase-angle compared to area A2 (Figure 5).

$$\begin{bmatrix} \Delta\omega_{A1} \\ \Delta V_{A1} \\ \Delta\omega_{A2} \\ \Delta V_{A2} \end{bmatrix} = -\underline{\mathbf{G}}_{4 \times 4}^{\text{no STAT}}(s) \begin{bmatrix} \Delta p_{A1} \\ \Delta q_{A1} \\ \Delta p_{A2} \\ \Delta q_{A2} \end{bmatrix} \quad (6)$$

$$\begin{aligned} \underline{\mathbf{G}}_{(1:2;1:2)}^{\text{no STAT}} &= \underline{\mathbf{K}}_g^{A1} \cdot (\underline{\mathbf{I}}_2 - \underline{\mathcal{C}}_g^{ia} \cdot (\underline{\mathbf{I}}_4 + \underline{\mathbf{S}}^{A1} \underline{\mathbf{K}}_g^{A1} \underline{\mathcal{C}}_g^{ia} + \underline{\mathbf{S}}^{A2} \underline{\mathbf{K}}_g^{A2} \underline{\mathcal{C}}_g^{ia})^{-1} \underline{\mathbf{S}}^{A1} \underline{\mathbf{K}}_g^{A1}) \\ \underline{\mathbf{G}}_{(1:2;3:4)}^{\text{no STAT}} &= \underline{\mathbf{K}}_g^{A1} \underline{\mathcal{C}}_g^{ia} \cdot (\underline{\mathbf{I}}_4 + \underline{\mathbf{S}}^{A1} \underline{\mathbf{K}}_g^{A1} \underline{\mathcal{C}}_g^{ia} + \underline{\mathbf{S}}^{A2} \underline{\mathbf{K}}_g^{A2} \underline{\mathcal{C}}_g^{ia})^{-1} \cdot \underline{\mathbf{S}}^{A2} \underline{\mathbf{K}}_g^{A2} \\ \underline{\mathbf{G}}_{(3:4;1:2)}^{\text{no STAT}} &= \underline{\mathbf{K}}_g^{A2} \underline{\mathcal{C}}_g^{ia} \cdot (\underline{\mathbf{I}}_4 + \underline{\mathbf{S}}^{A1} \underline{\mathbf{K}}_g^{A1} \underline{\mathcal{C}}_g^{ia} + \underline{\mathbf{S}}^{A2} \underline{\mathbf{K}}_g^{A2} \underline{\mathcal{C}}_g^{ia})^{-1} \cdot \underline{\mathbf{S}}^{A1} \underline{\mathbf{K}}_g^{A1} \\ \underline{\mathbf{G}}_{(3:4;3:4)}^{\text{no STAT}} &= \underline{\mathbf{K}}_g^{A2} \cdot (\underline{\mathbf{I}}_2 - \underline{\mathcal{C}}_g^{ia} \cdot (\underline{\mathbf{I}}_4 + \underline{\mathbf{S}}^{A1} \underline{\mathbf{K}}_g^{A1} \underline{\mathcal{C}}_g^{ia} + \underline{\mathbf{S}}^{A2} \underline{\mathbf{K}}_g^{A2} \underline{\mathcal{C}}_g^{ia})^{-1} \underline{\mathbf{S}}^{A2} \underline{\mathbf{K}}_g^{A2}) \end{aligned} \quad (7)$$

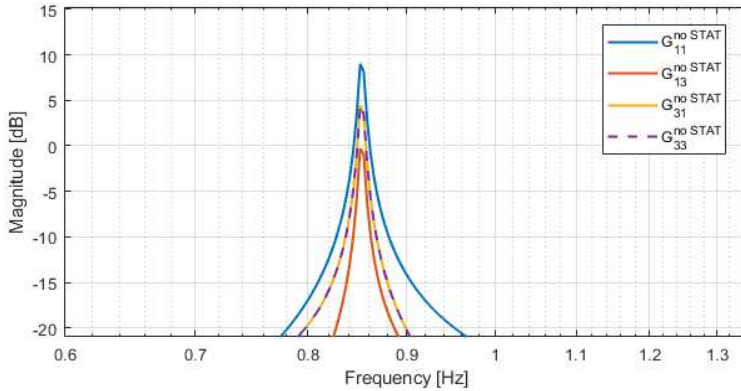


Fig. 5: Analytical assessment of the areas potentially more subjected to larger phase-angle variations.

Consider now the extension of the base case through the E-STATCOM installation. The impact can be modelled as additional feedbacks between the local area quantities $\Delta\omega_{Ai} / \Delta V_{Ai}$ and the converter active / reactive power contributions $\Delta p_{Ai}^c / \Delta q_{Ai}^c$. For this analysis, the well-known Virtual Synchronous Machine approach (VSM) will be deployed for the E-STATCOMs grid-forming control, whose synchronization mechanism is reported in Figure 6-a. Still, it is important to highlight that the positive effect associated to the E-STATCOM installation is independent with respect to the chosen grid-forming scheme and any alternative control configuration can be assessed in the light of the same proposed methodology.

By applying the linearization of the converter synchronization according to [9], it is possible to derive the equivalent MIMO system associated to the E-STATCOM (Figure 6-b). In this specific case, no explicit AC-voltage controller is included in the modeling; still, the proposed approach can be further extended to account also for the additional loops in the control.

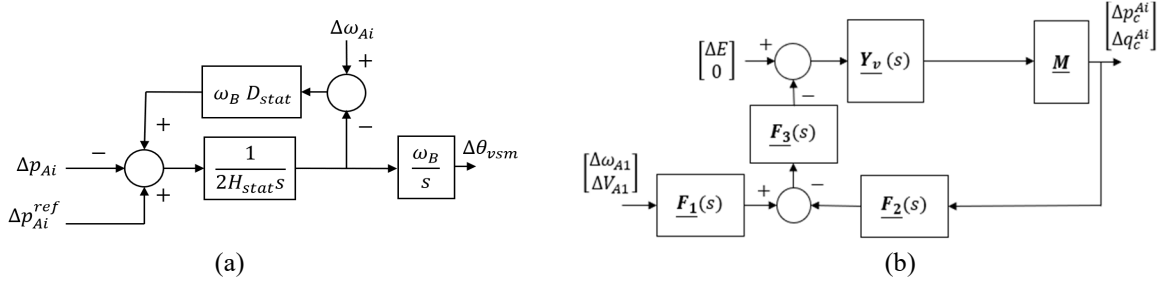


Fig. 6: Synchronization mechanism for the VSM system (a) and E-STATCOM control system MIMO representation for the assessment of its impact on inter-area phenomena (b); ΔE in (b) represents the variation of the back-EMF magnitude, assumed constant in this case.

The full E-STATCOM behavior is thus expressed in (8): the definition of the transfer matrix \underline{F}_1 , \underline{F}_2 and \underline{F}_3 can be derived combining the VSM synchronization system in Fig.6-a with the linearization approach from reference [9]; $\Delta\theta_{vsm}$ in Fig.6.a represents the converter synchronization angle used for the application of the linearization approach from [9].

$$\begin{bmatrix} \Delta p_{Ai}^c \\ \Delta q_{Ai}^c \end{bmatrix} = \underline{F}^{stat} \begin{bmatrix} \Delta\omega_{Ai} \\ \Delta V_{Ai} \end{bmatrix} = -(\underline{I}_{2 \times 2} - \underline{M} \underline{Y}_v \underline{F}_3 \underline{F}_2)^{-1} (\underline{M} \underline{Y}_v \underline{F}_3 \underline{F}_1) \begin{bmatrix} \Delta\omega_{Ai} \\ \Delta V_{Ai} \end{bmatrix} \quad (8)$$

$$\underline{Y}_v(s) = \begin{bmatrix} R_v + \frac{s}{\omega_B} L_v & -X_v \\ X_v & R_v + \frac{s}{\omega_B} L_v \end{bmatrix}^{-1} \quad \underline{M} = \frac{S_c}{S_b} \begin{bmatrix} 1 & 0 \\ 0 & -1 \end{bmatrix} \quad (9)$$

The introduction of the E-STATCOM effects \underline{F}^{stat} changes the characteristics of the local areas in Figure 3-b: the transfer matrixes \underline{K}_g^{Ai} modify in $\underline{K}_g^{Ai \text{ mod}}$ to account for the E-STATCOM effects:

$$\underline{K}_g^{Ai \text{ mod}}(s) = (\underline{I}_{2 \times 2} - \underline{K}_g^{Ai} \underline{F}^{stat})^{-1} \cdot \underline{K}_g^{Ai}(s) \quad (10)$$

The global network characteristics change according to the new transfer matrix $\underline{G}_{4 \times 4}^{\text{STAT}}$, which is formally equal to (7) but is now calculated deploying the modified area characteristics $\underline{K}_g^{Ai \text{ mod}}(s)$ instead of the original ones $\underline{K}_g^{Ai}(s)$, to account for the effects of the E-STATCOMs installation in the two areas.

E-STATCOM impact assessment: Oscillation damping.

Figure 7 and Figure 8 show respectively the time profiles associated to the network quantities in the base case where no E-STATCOMs are considered (Fig.7), and once E-STATCOM devices are connected at both sides of the two-area network (Fig.8). At a first glance, it is possible to appreciate the substantial reduction of the inter-area oscillations following a 50% variation of the local load connected to area A1. The presence of the E-STATCOMs helps toward the damping of the oscillatory phenomena in the measured local frequency profiles both for the area A1 and the area A2, improves the nadir of the transients (both for the frequencies and local voltages) and smoothens the profiles of the active / reactive power injections associated to the nearby synchronous machines.

Figure 9 shows the comparison of the theoretical model developed in the previous section against the spectral analysis of the time series from Figure 7 – Figure 8 (without and with E-STATCOM respectively). According to the theoretical model, the installation of the E-STATCOM devices is expected to induce a positive damping effect on the inter-area modes due to the reduction of the resonance peak around 0.7 Hz (see Fig. 9 - a); this result is confirmed by the reduction of the spectral components in the same frequency range as obtained from the simulations.

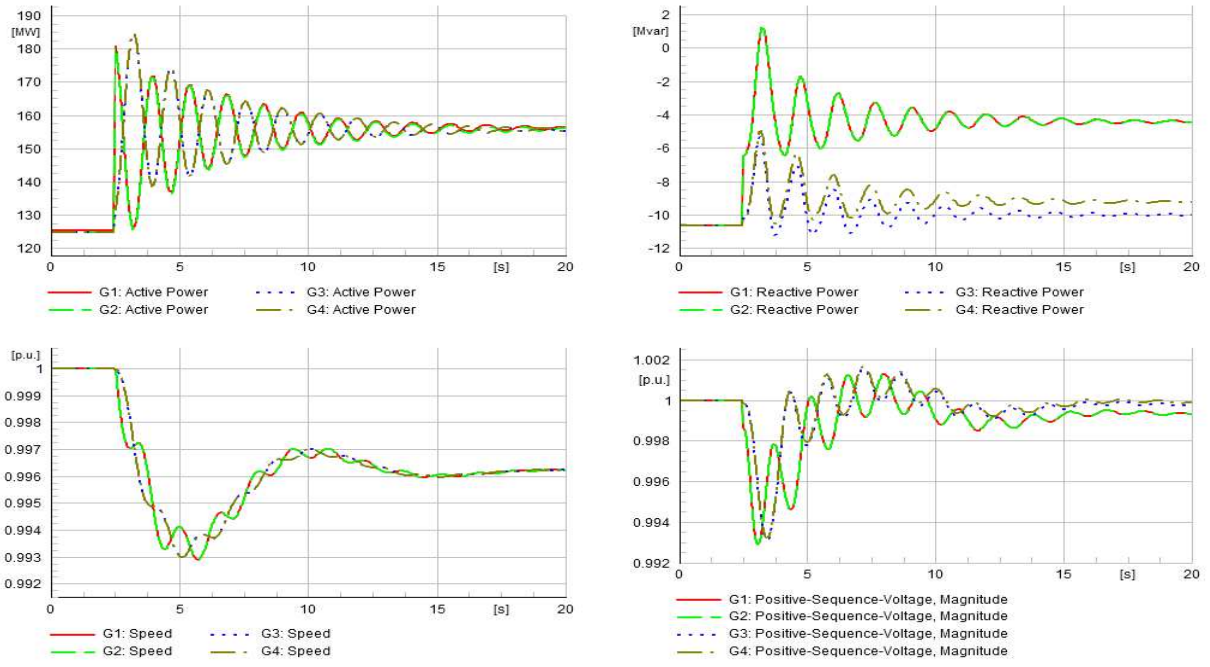


Fig. 7: Time profiles of the main generators' quantities (active / reactive power, angular frequency, and voltage magnitude) for the **BASE CASE**.

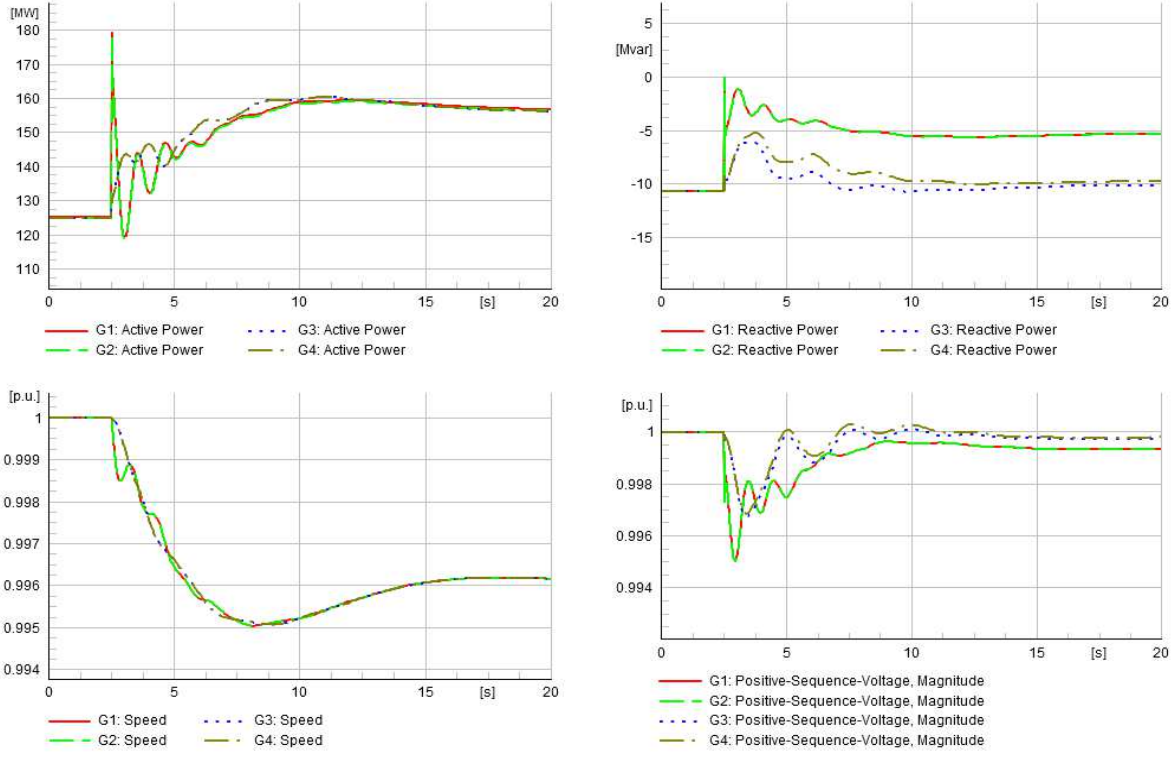


Fig. 8: Time profiles of the main generators' quantities (active / reactive power, angular frequency, and voltage magnitude, STATCOM active / reactive power) for the case with **both E-STATCOM 1 / E-STATCOM 2** connected.

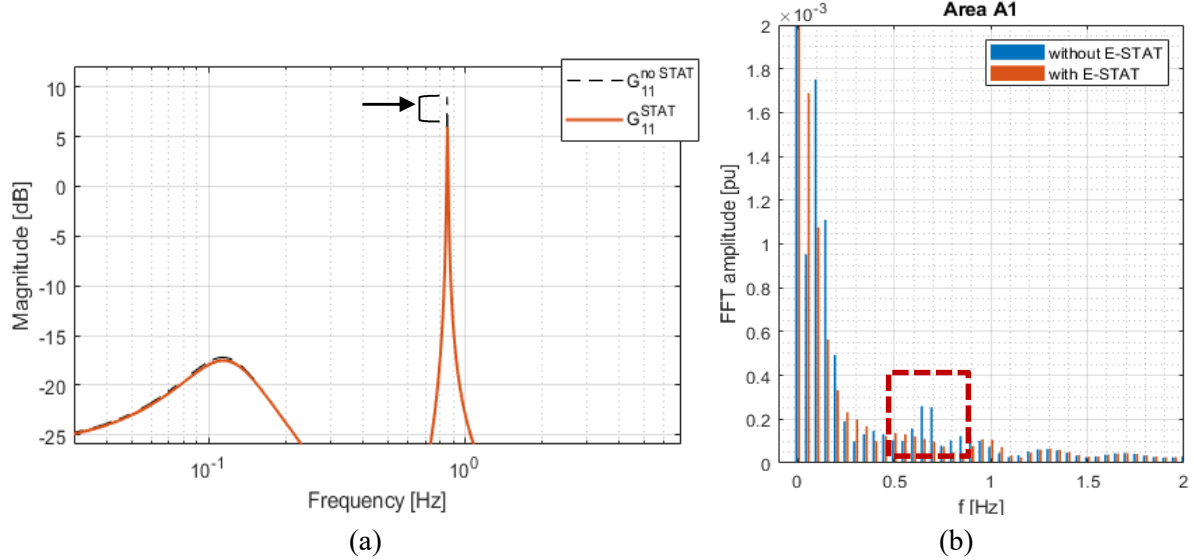


Fig. 9: (a) theoretical damping effect of the inter-area dynamics obtained from the analytical model and (b) measured impact of this effect on the local frequency spectrum for area A1.

E-STATCOM impact assessment: Placement.

Figures 10 and 11 show the effect of the E-STATCOM placement, assuming that just one unit may be placed into the network (either E-STATCOM 1 or E-STATCOM 2). This allows to derive insights in the best location for these elements. Figure 10 shows the frequency profiles once a 50% increase of the active load connected to area A1 is assumed as operating scenario; this scenario is evaluated both for the single-unit placement in area A1 (Figure 10-a) or in area A2 (Figure 10-b). A similar approach is considered in Figure 11, but in this case the load variation is applied to area A2.

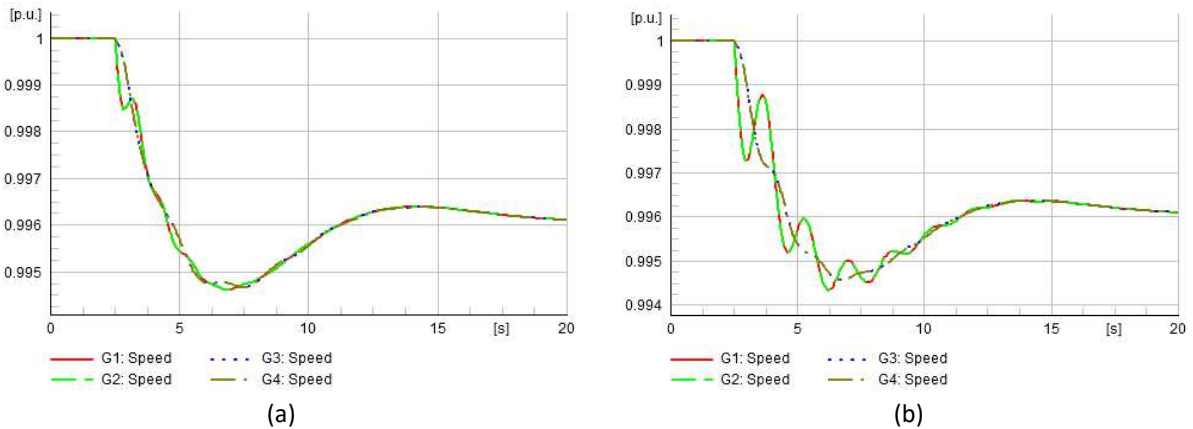


Fig. 10: Time profiles of the local angular frequencies for the case with (a) just E-STATCOM 1 connected and (b) just E-STATCOM 2 connected. Both cases are tested assuming the load variation in area A1 as the source of the inter-area event.

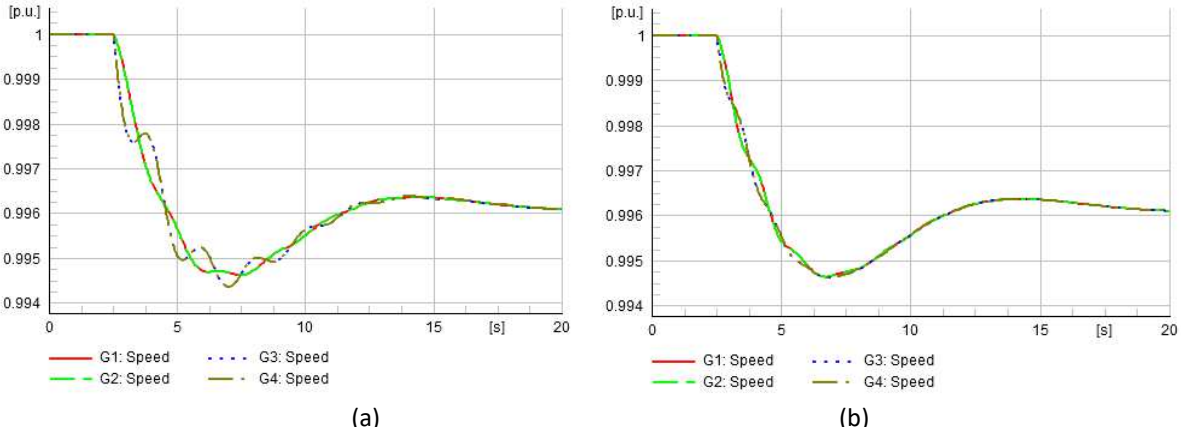


Fig. 11: Time profiles of the local angular frequencies for the case with (a) just E-STATCOM 1 connected and (b) just E-STATCOM 2 connected. Both cases are tested assuming load variation in area A2 as the source of the inter-area event.

The following considerations can be derived:

- For each of the considered load scenarios (Figure 10 and Figure 11 separately), the location of the E-STATCOM device close to the source of the disturbance provides the better results; that is, case (a) for Figure 10 and case (b) for Figure 11. If the source of the disturbance is known, the optimal location of the E-STATCOM is as close as possible to the origin of the oscillation.
- In case the source of the event is unknown (which is normally the case) and assuming no statistic difference in the size / likelihood of the disturbance events at the two sides of the network, the worst-case condition in Fig. 10 – b (considering both Figure 10 and Figure 11 together) indicates A1 as the more sensitive location for inter-area phase-angle fluctuations. This result is consistent with the analytical derivation in Fig. 5, confirms the correctness of the proposed approach, and provides useful insights on the areas to strengthen through larger E-STATCOM installations.

Conclusion

In this paper, the positive effect associated to E-STATCOM devices installation toward the damping of inter-area phenomena has been demonstrated and an analytical methodology based on MIMO characterization is proposed to predict the main dynamics of the system. The results (both at an analytical and simulated level) confirm the positive impact of E-STATCOM devices toward the stabilization of inter-area dynamics and provide useful insights in the optimal placement of these units.

References

- [1] P. Kundur et al., "Definition and classification of power system stability IEEE/CIGRE joint task force on stability terms and definitions," in IEEE Trans. on Power Systems, vol. 19, no. 3, pp. 1387-1401, Aug. 2004
- [2] S. A. N. Sarmadi and V. Venkatasubramanian, "Inter-Area Resonance in Power Systems from Forced Oscillations," in IEEE Transactions on Power Systems, vol. 31, no. 1, pp. 378-386, Jan. 2016
- [3] Y. Yu, and oth., "Oscillation Energy Analysis of Inter-Area Low-Frequency Oscillations in Power Systems," in IEEE Transactions on Power Systems, vol. 31, no. 2, pp. 1195-1203, March 2016.
- [4] M. J. Morshed and A. Fekih, "A Coordinated Controller Design for DFIG-Based Multi-Machine Power Systems," in IEEE Systems Journal, vol. 13, no. 3, pp. 3211-3222, Sept. 2019.
- [5] S. Yari and M. Khatibi, "Damping Improvement of Inter-Area Oscillations Using Large-Scale Wind Farms," 7th Iran Wind Energy Conference (IWEC2021), 2021, pp. 1-5.
- [6] I. Zenelis, X. Wang and I. Kamwa, "Online PMU-Based Wide-Area Damping Control for Multiple Inter-Area Modes," in IEEE Transactions on Smart Grid, vol. 11, no. 6, pp. 5451-5461, Nov. 2020.
- [7] P. Kundur, "Power System stability and control", Mc. Graw Hill, 1993, pp. 810.
- [8] A. Venkatraman, U. Markovic, et al., "Improving Dynamic Performance of Low-Inertia Systems Through Eigensensitivity Optimization," in IEEE Trans. on Power Systems, vol. 36, no. 5, pp. 4075-4088, Sept. 2021.
- [9] A. Bolzoni, "Generalized Nyquist MIMO Stability of Frequency Regulation Services in Power Networks," 2020 IEEE 21st Workshop on Control and Modeling for Power Electr. (COMPEL), 2020, pp. 1-7.